

# Thermodynamic Behavior of Excitonic Emission Properties in Manganese- and Zinc-Codoped Indium Phosphide Diluted Magnetic Semiconductor Layers

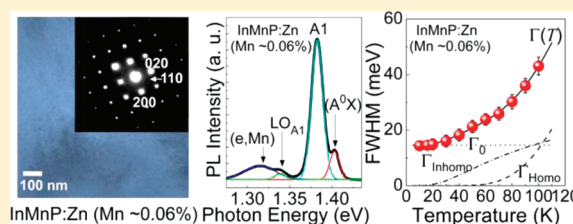
Sejoon Lee,<sup>†,‡</sup> Emil B. Song,<sup>‡</sup> Kang L. Wang,<sup>‡</sup> Chong S. Yoon,<sup>§</sup> Im Taek Yoon,<sup>†</sup> Yoon Shon,<sup>\*,†</sup> and Tae Won Kang<sup>\*,†</sup>

<sup>†</sup>Quantum-Functional Semiconductor Research Center, Dongguk University—Seoul, Seoul 100-715, Korea

<sup>‡</sup>Department of Electrical Engineering, University of California at Los Angeles, Los Angeles, California 90095, United States

<sup>§</sup>Division of Materials Science and Engineering, Hanyang University, Seoul 133-791, Korea

**ABSTRACT:** The thermodynamic behavior of excitonic emission properties in manganese- and zinc-codoped indium phosphide (InMnP:Zn) diluted magnetic semiconductor (DMS) layers was investigated. Compared to the InMnP:Zn DMS layer (Mn  $\approx$  0.06%), the inhomogeneous thermal-broadening of the excitonic-emission line-width in InMnP:Zn DMS layer (Mn  $\approx$  0.29%) is dominant at lower temperatures. This is attributed to the increase of ionized impurity scattering from Mn ions and results in the increase of exciton–phonon coupling strength. As a consequence, high Mn content can lead to low excitonic emission efficiency, although generally a larger Mn content is favorable to increase the Curie temperature of a DMS material.



## 1. INTRODUCTION

The diluted magnetic semiconductor (DMS) has emerged as the most promising candidate for spintronic applications.<sup>1–7</sup> In the past decade, numerous theoretical and experimental studies on the physical properties of DMSs have been extensively conducted in III–V systems (GaAs, InAs, GaN, and InP).<sup>8–29</sup> Furthermore, in recent years, spintronic devices such as spin field-effect transistor and spin-polarized light-emitting diode (spin-LED) have been experimentally demonstrated.<sup>4,5</sup> Although multiple spin functionalities have been observed, the devices show extremely low efficiency. For spin-LED, the electroluminescence efficiency is low and is strongly affected by the spin-lifetime and excitonic properties. While the spin-lifetime depends on the ferromagnetic property of the DMS, the excitonic emission relies on the interactions with phonons. Since DMSs generally require low temperature growth conditions to suppress cluster formation, the crystallinity becomes poor compared to conventional semiconductors, and thus results in an increased exciton–phonon interaction. Moreover, the magnetic dopants responsible for ferromagnetism in DMSs are intimately correlated with the excitonic emission property.

In this work, we examine the thermodynamic behavior of excitonic emission properties in manganese- and zinc-codoped indium phosphide (InMnP:Zn) DMS layers by temperature-dependent photoluminescence (PL) measurements below the ferromagnetic transition temperature ( $T_C$ ). The exciton–phonon interaction is analyzed by comparing the experimental PL parameters with theoretical models, which takes into account both the Bose–Einstein statistics<sup>30</sup> and Fröhlich interaction.<sup>31</sup>

## 2. EXPERIMENTAL SECTION

The 3- $\mu$ m thick *p*-type Zn-doped InP epilayers with hole concentration of  $>10^{18}$  cm<sup>−3</sup> were grown on semi-insulating (001) InP substrates by metal–organic chemical vapor deposition (MOCVD) using trimethylindium (TMIn), diethylzinc (DEZn), and phosphine (PH<sub>3</sub>) sources at 650 °C. After deoxidizing the sample surface at 500 °C, high purity Mn (99.9999%) was evaporated onto the *p*-InP:Zn epilayers by molecular beam epitaxy (MBE) in ultra high vacuum ( $\sim 10^{-10}$  Torr) at room temperature for 30–180 s. Then, the samples were subsequently annealed at 300 °C for 30 min in N<sub>2</sub>. After thermal annealing, the thicknesses of InMnP:Zn DMS layers were confirmed to be  $\sim 30$ –50 nm by Auger electron spectroscopy. The InMnP:Zn epilayers showed *p*-type conductivity with hole concentration of  $\sim 10^{19}$  cm<sup>−3</sup> from Hall effect measurements at room temperature.

Structural and microstructural properties of InMnP:Zn epilayers were monitored by high-resolution X-ray diffraction (HR-XRD) and transmission electron microscopy (TEM) measurements, respectively. Temperature-dependent PL measurements were carried out using a 75 cm monochromator with an RCA31034 photomultiplier tube and an excitation He–Ne laser source of 632.8 nm at 10–100 K. In order to investigate the effect of Mn content on the excitonic properties, two types of InMnP:Zn DMS layers (Mn  $\approx$  0.06% and  $\approx$  0.29%) showing clear ferromagnetism ( $T_C \approx 100$ –150 K)<sup>22</sup> were examined in this

**Received:** August 16, 2011

**Revised:** October 19, 2011

**Published:** October 21, 2011

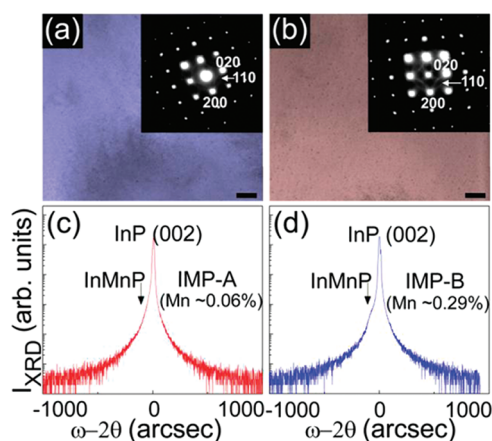


**Figure 1.** Bright-field TEM images and SAED patterns of (a) IMP-A (scale bar = 100 nm) and (b) IMP-B (scale bar = 100 nm). XRD spectra of (c) IMP-A and (d) IMP-B.

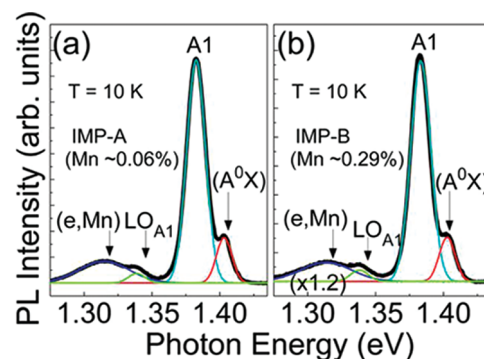
study. And, for convenience, we denote the two samples as IMP-A ( $\text{Mn} \approx 0.06\%$ ) and IMP-B ( $\text{Mn} \approx 0.29\%$ ). The Mn contents of both samples were confirmed by X-ray photoelectron spectroscopy.

### 3. RESULTS AND DISCUSSION

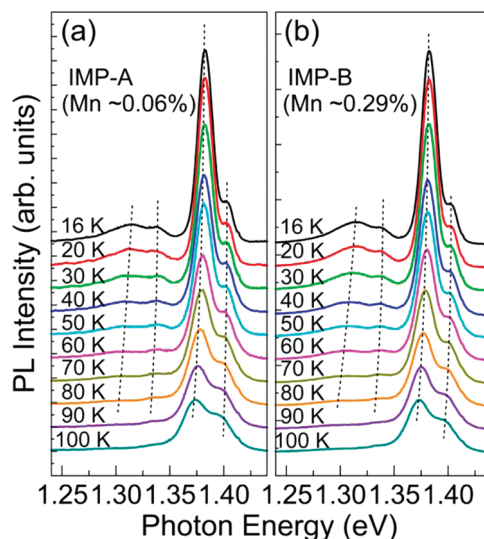
Figure 1 shows bright-field TEM images of IMP-A and IMP-B. The IMP-A shows no visible particles; however, the IMP-B contains numerous particles with the size of  $<10$  nm. In order to examine the existence of secondary phases, the selective-area electron diffraction (SAED) patterns were measured. As shown in the insets of Figure 1a,b, the SAED patterns of both IMP-A and IMP-B demonstrate a 001 zone of single-crystalline InP. The pattern, however, contains faint ring-patterns corresponding to the  $P_{4/2}/mmm$  structure of  $\text{MnO}_2$  ( $a = 4.4 \text{ \AA}$ ,  $c = 2.9 \text{ \AA}$ ), which is likely to be formed during the thermal treatment. Diffraction patterns of different lattice phases are not observed, which indicates that no other magnetic phases containing Mn, In, or P were nucleated in the samples. The SAED pattern shows that the Mn additives are well incorporated in the InP lattices (see also the HR-XRD spectra of IMP-A and IMP-B in Figures 1c,d, respectively).

Figure 2 displays the PL spectra of IMP-A and IMP-B at 10 K. For both samples, four relevant PL features are clearly noticeable. The peaks at 1.40, 1.38, 1.34, and 1.32 eV denoted by ( $\text{A}^0\text{X}$ ), A1,  $\text{LO}_{\text{A1}}$ , and (e,Mn) correspond to the neutral acceptor bound exciton, the unidentified carbon-related donor–acceptor pair transition,<sup>22</sup> the first phonon replica of A1, and the Mn-related emission, respectively. In III–V DMSs, the (e,Mn) peak originates from the neutral Mn acceptor [i.e.,  $\text{A}^0 + h\nu \rightarrow \text{A}^- + h^+ \rightleftharpoons \text{Mn}_{\text{III}}^{3+}(3d^4) + e^- + h^+ \rightarrow \text{Mn}_{\text{III}}^{2+}(3d^5) + h^+$ , where  $\text{A}^0$  and  $\text{A}^-$  are neutral acceptor and ionized acceptor, respectively].<sup>32,33</sup> Thus, the appearance of both (e,Mn) and ( $\text{A}^0\text{X}$ ) indicates that the substitutionally incorporated Mn ions are acting as acceptors, which is further corroborated by the observation of hole-induced ferromagnetism in our previous work.<sup>22</sup>

Here, it should be noted that the large number of incorporated magnetic ions leads to the distortion of the energy dispersions in the solid-state lattice, and results in an increase of phonon- and/or impurity-scattering, which strongly relates to the exciton–phonon interaction. Therefore, in order to examine the Mn



**Figure 2.** PL spectra of (a) IMP-A and (b) IMP-B at 10 K. The red, green, blue, and cyan lines are the best-fitted curves.



**Figure 3.** Temperature-dependent PL spectra of (a) IMP-A and (b) IMP-B at 16–100 K.

content-dependence of the thermodynamic PL emission properties, we measure the temperature-dependence of the PL for both IMP-A and IMP-B samples, especially below  $T_C$ . Figure 3 shows the temperature-dependence of the PL spectra for IMP-A and IMP-B at 16–100 K. In both samples, as the temperature increases, (e,Mn) and ( $\text{A}^0\text{X}$ ) become quenched and show a red-shift. The temperature-dependent red-shift of the acceptor-related emission bands reveals the strength of the phonon–exciton interaction and is further discussed below.

According to the Bose–Einstein approximation,<sup>30</sup> the temperature-dependence of the excitonic emission energy can be represented by the effective phonon energy  $\hbar\omega_{\text{eff}}$  and the exciton–phonon coupling strength  $\lambda$ . The relationship is given by the following:

$$E(T) = E(0) - \lambda / [\exp(\hbar\omega_{\text{eff}}/k_B T) - 1] \quad (1)$$

where  $E(0)$ ,  $k_B$ , and  $T$  are the exciton resonance energy at  $T = 0$  K, the Boltzmann constant, and the measurement temperature, respectively. Figure 4 shows the variation of the ( $\text{A}^0\text{X}$ ) emission energy as a function of the temperature. By inserting the experimental PL parameters into eq 1, the  $\lambda$  and  $\hbar\omega_{\text{eff}}$  are extracted to be 26 and 13.1 meV for IMP-A and 31 and 16.4 meV for IMP-B, respectively. These values are comparable to those

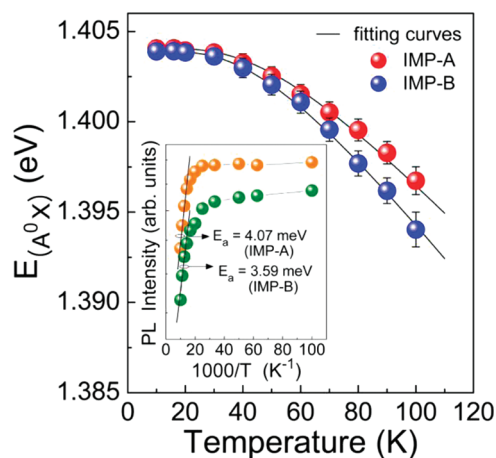


**Figure 4.** Variation of ( $A^0X$ ) emission energy as a function of the measurement temperature of IMP-A and IMP-B. The inset shows the variation of the relative PL intensity of ( $A^0X$ ) emission as a function of the inverse temperature for both samples. Symbols represent experimental data, and solid lines are fitting-curves of Bose–Einstein approximation.

in the host InP.<sup>34</sup> However,  $\lambda$  and  $\hbar\omega_{\text{eff}}$  of IMP-B are slightly larger than those of IMP-A, which indicates the exciton–phonon coupling in IMP-B is stronger than that in IMP-A. The error bars are also shown in Figure 4. The error rates corresponding to “multiple Gaussian fitting” are less than  $\pm 0.5\%$  for multiple samples, which indicates that the extracted parameters are reliable.

The difference of the exciton–phonon coupling in both samples can be explained as a difference in the exciton activation energy ( $E_a$ ). The temperature-dependence of the excitonic emission energy is primarily related to the thermal expansion of the excitonic radiative-recombination. The activation energy of  $E_a$  is given by the following:<sup>35</sup>

$$I = I_0 / [1 + A \cdot \exp(-E_a/k_B T)] \quad (2)$$

where  $I_0$  and  $A$  are the PL intensity at 0 K and the fitting parameter, respectively. As shown in the inset of Figure 4, the extracted  $E_a$  is  $4.07 \pm 0.04$  meV for IMP-A and  $3.59 \pm 0.03$  meV for IMP-B. These values are in good agreement with the literature<sup>36</sup> but are slightly lower, in particular for IMP-B. The discrepancy arises from an increased thermal dissociation of ( $A^0X$ ), which is caused by the increase of impurity scattering from the large number of Mn ions.

In order to clarify the origin of the decreased  $E_a$  in terms of the exciton–phonon coupling, we evaluate the thermal broadening of the excitonic emission line width. The temperature dependence of the exciton emission’s full-width at half-maximum (fwhm) can be interpreted through both intrinsic and extrinsic factors, which promote the dissociation of excitons. The intrinsic factor of homogeneous broadening ( $\Gamma_{\text{Homo}}$ ) is due to the dissociation of excitons by means of collision with the phonons, while the extrinsic factor of inhomogeneous broadening ( $\Gamma_{\text{Inhomo}}$ ) is due to the dissociation of excitons by ionized impurity scattering.<sup>31,37–39</sup> This relationship is given by the following:<sup>37</sup>

$$\Gamma(T) = \Gamma_{\text{Homo}} + \Gamma_{\text{Inhomo}} = \Gamma_{\text{AC}}T + \Gamma_{\text{LO}} / [\exp(\theta_{\text{LO}}/T) - 1] + \Gamma_I \exp(-E_I/k_B T) + \Gamma_0 \quad (3)$$

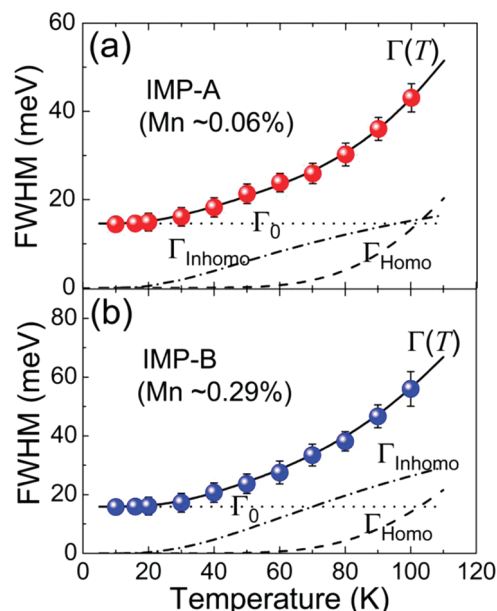


**Figure 5.** Variation in fwhm of ( $A^0X$ ) emission for (a) IMP-A and (b) IMP-B. Symbols represent experimental data, and lines (solid, dashed, dotted, and dot-dashed lines) are fitting-curves of the Fröhlich model.

where  $\Gamma_{\text{AC}}$ ,  $\Gamma_{\text{LO}}$ , and  $\theta_{\text{LO}}$  in the first and second terms [ $=\Gamma_{\text{Homo}}$ ] of eq 3 are the exciton–acoustic phonon coupling strength, the exciton–longitudinal optical (LO) phonon coupling strength, and the average energy of LO phonons contributing to the Fröhlich interaction (scattering events), respectively. In the third term [ $=\Gamma_{\text{Inhomo}}$ ] of eq 3,  $\Gamma_I$  and  $E_I$  are the broadening factor of the fully ionized impurity scattering and the average binding energy of impurities, respectively. The last term  $\Gamma_0$  in eq 3 is the zero-temperature broadening parameter corresponding to the intrinsic and extrinsic factors, such as the Auger process, the intrinsic exciton lifetime, and the electron–electron interaction.

Figure 5 displays the variations of FWHMs as a function of the temperature for IMP-A and IMP-B. The average error rates due to “multiple Gaussian fitting” are less than  $\pm 4\%$  for multiple samples, and the obtained FWHMs are fitted well by eq 3. Here, we used  $\theta_{\text{LO}}$  of 496 K for the LO phonon energy ( $= 43$  meV) of the host InP<sup>39</sup> and  $\Gamma_{\text{AC}}$  of  $4 \times 10^{-4}$  meV/K. The extracted values of  $\Gamma_{\text{LO}}$ ,  $\Gamma_I$ , and  $E_I$  are 694 meV, 38 meV, and 8.1 meV for IMP-A and 709 meV, 85 meV, and 10.0 meV for IMP-B, respectively. Based on the results, we can conjecture that  $\Gamma_I$  (i.e., impurity scattering) is larger for IMP-B in comparison with IMP-A. This feature can also be confirmed from the individual fitting-curves of  $\Gamma_{\text{Homo}}$  and  $\Gamma_{\text{Inhomo}}$ . As can be seen from Figures 5a and 5b, the best-fitted curves demonstrate that  $\Gamma_{\text{Inhomo}}$  is different in each sample, while  $\Gamma_{\text{Homo}}$  is similar. Namely,  $\Gamma_{\text{Inhomo}}$  is dominant above  $\sim 70$  K for IMP-B and  $\sim 100$  K for IMP-A. This depicts that the extrinsic factor of  $\Gamma_{\text{Inhomo}}$  for IMP-B (high Mn contents) is greater than IMP-A (low Mn contents), which is associated with the increase of impurity scattering. As a consequence, high Mn content can lead to low excitonic emission efficiency, although generally a larger Mn content below the solubility limit is favorable to increase the  $T_C$  of a DMS material.

#### 4. CONCLUSIONS

The thermodynamic behavior of excitonic emission properties in InMnP:Zn DMS layers was investigated. The InMnP:Zn



DMS layers were prepared by a thermal diffusion process at 300 °C using a bulk diffusion couple of MBE-grown Mn on MOCVD-grown *p*-InP:Zn, and the exciton–phonon interaction was characterized through temperature-dependent PL measurements. The exciton–phonon coupling in the InMnP:Zn DMS layer with higher Mn contents (~0.29%) was estimated to be slightly larger than the InMnP:Zn DMS layer with lower Mn contents (~0.06%), which causes the decrease in exciton activation energy. This comes from the enhanced  $\Gamma_{\text{Inhom}}$ , which means the large number of incorporated Mn ions increases the impurity scattering and gives rise to the dissociation of excitons.

## AUTHOR INFORMATION

### Corresponding Author

\*Tel: +82-2-2260-3205; Fax: +82-2-2260-3945; E-mail: twkang@dongguk.edu (T.W.K.); sonyun@dongguk.edu (Y.S.).

## ACKNOWLEDGMENT

This research was supported by the National Research Foundation Grant (Grant Nos. NRF-2011-0000016, NRF-K20902001603-10E0100-04010, K20902001819-10B1200-23110, and KRF-2008-313-C00264) funded by the Korean government of Ministry of Education, Science and Technology (MEST).

## REFERENCES

- (1) Prinz, G. *Science* **1998**, *282*, 1660–1663.
- (2) Awschalom, D. D.; Kawakami, R. K. *Nature* **2000**, *408*, 923–924.
- (3) Wolf, S. A.; Awschalom, D. D.; Buhrman, R. A.; Daughton, J. M.; von Molnár, S.; Roukes, M. L.; Chhelkanova, A. Y.; Treger, D. M. *Science* **2001**, *294*, 1488–1495.
- (4) Awschalom, D. D.; Loss, D.; Samarth, N., Eds. *Semiconductor Spintronics and Quantum Computation*; Springer: New York, 2002.
- (5) Žutić, I.; Fabian, J.; Sarma, S. D. *Rev. Mod. Phys.* **2004**, *76*, 323–410.
- (6) Ohno, H. *Science* **1998**, *281*, 951–956.
- (7) Dietl, T.; Ohno, H.; Matsukura, F.; Cibert, J.; Ferrand, D. *Science* **2000**, *287*, 1019–1022.
- (8) Ohno, H.; Chiba, D.; Matsukura, F.; Omiya, T.; Abe, E.; Dietl, T.; Ohtani, K. *Nature* **2000**, *408*, 944–946.
- (9) Tanaka, M.; Higo, Y. *Phys. Rev. Lett.* **2001**, *87*, 026602.
- (10) Sapra, S.; Sarma, D. D.; Sanvito, S.; Hill, N. A. *Nano Lett.* **2002**, *2*, 605–608.
- (11) Shon, Y.; Lee, W. C.; Park, Y. S.; Kwon, Y. H.; Lee, S. J.; Chung, K. J.; Kim, H. S.; Kim, D. Y.; Fu, D. J.; Kang, T. W.; Fan, X. J.; Park, Y. J.; Oh, H. T. *Appl. Phys. Lett.* **2004**, *84*, 2310–2312.
- (12) Somaskandan, K.; Tsoi, G. M.; Wenger, L. E.; Brock, S. L. *Chem. Mater.* **2005**, *17*, 1190–1198.
- (13) Sahoo, Y.; Poddar, P.; Srikanth, H.; Lucey, D. W.; Prasad, P. N. *J. Phys. Chem. B* **2005**, *109*, 15221–15225.
- (14) Radovanovic, P. V.; Barrelet, C. J.; Gradecak, S.; Qian, F.; Lieber, C. M. *Nano Lett.* **2005**, *5*, 1407–1411.
- (15) Xiangyang, H.; Makmal, A.; Chelikowsky, J. R.; Kronik, L. *Phys. Rev. Lett.* **2005**, *94*, 236801.
- (16) Poddar, P.; Sahoo, Y.; Srikanth, H.; Prasad, P. N. *Appl. Phys. Lett.* **2005**, *87*, 062506.
- (17) Shon, Y.; Lee, S.; Jeon, H. C.; Lee, S.-W.; Kim, D. Y.; Kang, T. W.; Kim, E. K.; Fu, D. J.; Yoon, C. S.; Kim, C. K. *Appl. Phys. Lett.* **2006**, *88*, 232511.
- (18) Shon, Y.; Lee, S.; Jeon, H. C.; Lee, S.-W.; Kim, D. Y.; Kang, T. W.; Kim, E. K.; Yoon, C. S.; Kim, C. K.; Park, Y. J.; Lee, J. J. *Appl. Phys. Lett.* **2006**, *89*, 041905.
- (19) Sadowski, J.; Dłuzewski, P.; Kret, S.; Janik, E.; Łusakowska, E.; Kanski, J.; Presz, A.; Terki, F.; Charar, S.; Tang, D. *Nano Lett.* **2007**, *7*, 2724–2728.
- (20) Schmidt, T. M. *Phys. Rev. B* **2008**, *77*, 085325.
- (21) Kim, J. S.; Kim, E. K.; Shon, Y.; Lee, S. *Appl. Phys. Lett.* **2008**, *93*, 242110.
- (22) Shon, Y.; Lee, S.; Kim, D. Y.; Kang, T. W.; Yoon, C. S.; Kim, E. K.; Lee, J. J. *New J. Phys.* **2008**, *10*, 115002.
- (23) Wurstbauer, U.; Sperl, M.; Soda, M.; Neumaier, D.; Schuh, D.; Bayreuther, G.; Zweck, J.; Wegscheider, W. *Appl. Phys. Lett.* **2008**, *92*, 102506.
- (24) Maccherozzi, F.; Sperl, M.; Panaccione, G.; Minar, J.; Polesya, S.; Ebert, H.; Wurstbauer, U.; Hochstrasser, M.; Rossi, G.; Woltersdorf, G.; Wegscheider, W.; Back, C. H. *Phys. Rev. Lett.* **2008**, *101*, 267201.
- (25) Kim, H. S.; Cho, Y. J.; Kong, K. J.; Kim, C. H.; Chung, G. B.; Park, J. *Chem. Mater.* **2009**, *21*, 1137–1143.
- (26) Rudolph, A.; Soda, M.; Kiessling, M.; Wojtowicz, T.; Schuh, D.; Wegscheider, W.; Zweck, J.; Back, C.; Reiger, E. *Nano Lett.* **2009**, *9*, 3860–3866.
- (27) Hilse, M.; Takagaki, Y.; Herfort, J.; Ramsteiner, M.; Herrmann, C.; Breuer, S.; Geelhaar, L.; Riechert, H. *Appl. Phys. Lett.* **2009**, *95*, 133126.
- (28) Bucsa, I. G.; Cochrane, R. W.; Roorda, S. J. *Appl. Phys.* **2010**, *107*, 073912.
- (29) Galicka, M.; Buczko, R.; Kacman, P. *Nano Lett.* **2011**, *11*, 3319–3323.
- (30) Lautenschlager, P.; Garriga, M.; Logothetidis, S.; Cardona, M. *Phys. Rev. B* **1987**, *35*, 9174–9189.
- (31) Rudin, S.; Reinecke, T. L.; Segall, B. *Phys. Rev. B* **1990**, *42*, 11218–11231.
- (32) Kreissl, J.; Ulrici, W.; El-Metoui, M.; Vasson, A.-M.; Vasson, A.; Gavaix, A. *Phys. Rev. B* **1996**, *54*, 10508–10515.
- (33) Szcztytko, J.; Twardowski, A.; Swiatek, K.; Palczewska, M.; Tanaka, M.; Hayashi, T.; Ando, K. *Phys. Rev. B* **1999**, *60*, 8304–8308.
- (34) Pavesi, L.; Piazza, F.; Rudra, A.; Carlin, J. F.; Ilegems, M. *Phys. Rev. B* **1991**, *44*, 9052–9055.
- (35) Jiang, D. S.; Jung, H.; Ploog, K. J. *Appl. Phys.* **1998**, *64*, 1371–1377.
- (36) Skromme, B. J.; Stillman, G. E. *Phys. Rev. B* **1983**, *28*, 4602–4607.
- (37) Chen, Y.; Kothiyal, G. P.; Singh, I.; Bhattacharya, P. K. *Superlattices Microstruct.* **1987**, *3*, 657–664.
- (38) Lyon, S. A. *J. Lumin.* **1986**, *35*, 121–154.
- (39) Perna, G.; Capozzi, V.; Lorusso, G. F.; Bruno, G.; Losurdo, M.; Capezzuto, P. *Semicond. Sci. Technol.* **2000**, *15*, 736–743.